Medicine in Novel Technology and Devices 13 (2022) 100113

Contents lists available at ScienceDirect

Medicine in Novel Technology and Devices

journal homepage: www.journals.elsevier.com/medicine-in-novel-technology-and-devices/

Full Length Article

Biomechanics of human optic chiasmal compression: *ex vivo* experiment and finite element modelling

Xiaofei Wang [a,b,*], Andrew J. Neely [b], Neeranjali S. Jain [c,d], Swaranjali V. Jain [c,d], Sanjiv Jain [e], Murat Tahtali [b], Gawn G. McIlwaine [f,g], Christian J. Lueck [c,h]

[a] *Laboratory for Biomechanics and Mechanobiology of Ministry of Education, Beijing Advanced Innovation Centre for Biomedical Engineering, School of Biological Science and Medical Engineering, Beihang University, Beijing, 100083, China*
[b] *School of Engineering and Information Technology, University of New South Wales, Canberra, Australian Capital Territory, Australia*
[c] *Department of Neurology, The Canberra Hospital, Canberra, Australian Capital Territory, Australia*
[d] *Faculty of Medicine, University of New South Wales, Kensington, Sydney, New South Wales, Australia*
[e] *Department of Anatomical Pathology, The Canberra Hospital, Canberra, Australian Capital Territory, Australia*
[f] *Queen's University Belfast, Belfast, Northern Ireland, UK*
[g] *Belfast Health and Social Care Trust, Belfast, Northern Ireland, UK*
[h] *Australian National University Medical School, Canberra, Australian Capital Territory, Australia*

ARTICLE INFO

Keywords:
Bitemporal hemianopia
Pituitary tumour
Chiasm
Finite element modelling
Optic nerve fibre

ABSTRACT

The mechanism of bitemporal hemianopia arising as a result of chiasmal compression is unknown. In this study, we combined an *ex vivo* experiment and finite element modelling (FEM) to investigate its potential mechanism. A cadaveric human optic chiasm was scanned using micro-CT before and after deformation by inflation of Foley catheter, to simulate tumour growth from beneath. The geometry of the same chiasm was reconstructed and simulated using finite element analysis. Chiasmal deformations were extracted from the simulation and compared with those observed during micro-CT scanning. In addition, nerve fibre models examining variation in local fibre distribution patterns of the chiasm were incorporated to investigate the strain (deformation) distributions of the chiasm at an axonal level. The FEM model matched the micro-CT scans well both qualitatively and quantitatively. Compression of the chiasm induced high strains in the paracentral portions of the chiasm where the crossing optic nerve fibres are located. At an axonal level, the magnitude of strains affecting crossed fibres were greater than those affecting uncrossed fibres. The high strains in the paracentral portions of the chiasm, combined with the differences in strain between crossed and uncrossed nerve fibres, are consistent with a biomechanical explanation for the pattern of visual field loss seen in chiasmal compression.

1. Introduction

Bitemporal hemianopia is a type of visual field (VF) defect in which vision is impaired in the temporal parts of the VFs of both eyes. Bitemporal hemianopia generally implies damage to the optic chiasm, specifically to fibres arising from the nasal hemiretinae which traverse the centre of the chiasm. It has many known causes but the most common is chiasmal compression from a pituitary tumour [1]. The precise mechanism of bitemporal hemianopia remains poorly understood. Previous theories suggesting that it arises from the effects of stretching [2] or alteration in blood supply [3] cannot explain the sharp cutoff along the vertical midline of the VFs which is observed clinically.

Biomechanical theories have been proposed to explain the pattern of VF loss seen in bitemporal hemianopia [1,4]. We have previously used finite element modelling (FEM) to simulate chiasmal compression in order to examine these biomechanical theories [5] [–] [7]. Preliminary results show that the biomechanics of the chiasmal compression may, at least in part, account for the predominant temporal VF loss.

However, in our previous models, the complex 3D structure of the chiasm was not represented in detail and the models have not been validated against experimental data. This study was therefore set up to improve our understanding of the mechanisms by which chiasmal compression causes bitemporal hemianopia with the following aims: 1) to perform an *ex vivo* experiment using micro-CT imaging to look at

* Corresponding author. Ophthalmic Engineering & Visual Science Laboratory, School of Biological Science and Medical Engineering, Beihang University, Room 424, Building 5, 37 Xueyuan Road, Beijing, 10083, China.
E-mail address: xiaofei.wang@buaa.edu.cn (X. Wang).

https://doi.org/10.1016/j.medntd.2021.100113
Received 22 December 2021; Received in revised form 31 December 2021; Accepted 31 December 2021
2590-0935/© 2022 The Author(s). Published by Elsevier B.V. This is an open access article under the CC BY-NC-ND license (http://creativecommons.org/licenses/by-nc-nd/4.0/).

chiasmal compression of a cadaveric optic chiasm; 2) to simulate the distribution of strain within the compressed chiasm using FEM and thereby validate the model against experimental data; 3) to investigate the influence of nerve fibre orientation on deformations of axons at a micro-scale level by incorporating detailed fibre distributions into the nerve fibre models [8].

2. Methods

We combined an *ex vivo* experiment and a FEM model to investigate the deformation of the optic chiasm at a macro level, and the strain experienced by nerve fibres at a micro level during compression.

2.1. Micro computed tomography (Micro-CT) imaging

This study was approved by the ACT Health Human Research Ethics Committee (ETH 1.14.020). The sample obtained was an optic chiasm harvested at autopsy from a 26-year-old male approximately 60 h after death. It was fixed in formalin (10% in phosphate buffer, pH 7.2).

A mounting apparatus consisting of four holders and a base was designed to allow compression of the chiasm from below (Fig. 1). The holders and base were custom-designed and 3D-printed to fit within the micro-CT scanner's bore. A 10 French gauge paediatric Foley catheter with a balloon capacity of 5 mL (Bard, West Sussex, UK) was used to elevate the chiasm, simulating compression by a tumour growing from below (Fig. 1). A hemispherical depression was created in the base to accommodate the Foley catheter balloon. Superglue (Uhu GmbH & Co. KG, Bühl, Germany) was used to bond the sectioned ends of the optic nerves and optic tracts to four holders which were then glued to the base. The four holders were placed on a horizontal surface before being glued to the base to prevent any torsion of the optic nerves or tracts. A syringe of water was used to inflate the balloon of the Foley catheter which was inserted into the depression in the base.

Micro-CT imaging of the undeformed chiasm. Imaging was performed using a Quantum FX micro-CT system (PerkinElmer Corporation, Massachusetts, USA). The optic chiasm, mounting apparatus and Foley catheter were positioned on the sample bed of a micro-CT scanner and the Foley catheter was secured to the base by insulating tape (Fig. 1). The field of view for image acquisition was set to be 30 mm, which was large enough to encompass the chiasm and give relatively high resolution of 59 μm/pixel. The position of the sample bed of the micro-CT was adjusted so that the volume of image acquisition was centred on the optic chiasm in all three planes.

The Foley catheter balloon was inflated so that it just touched the optic chiasm without inducing any deformation after which the setup was scanned. Scanning time was 3 min, during which 512 separate slices

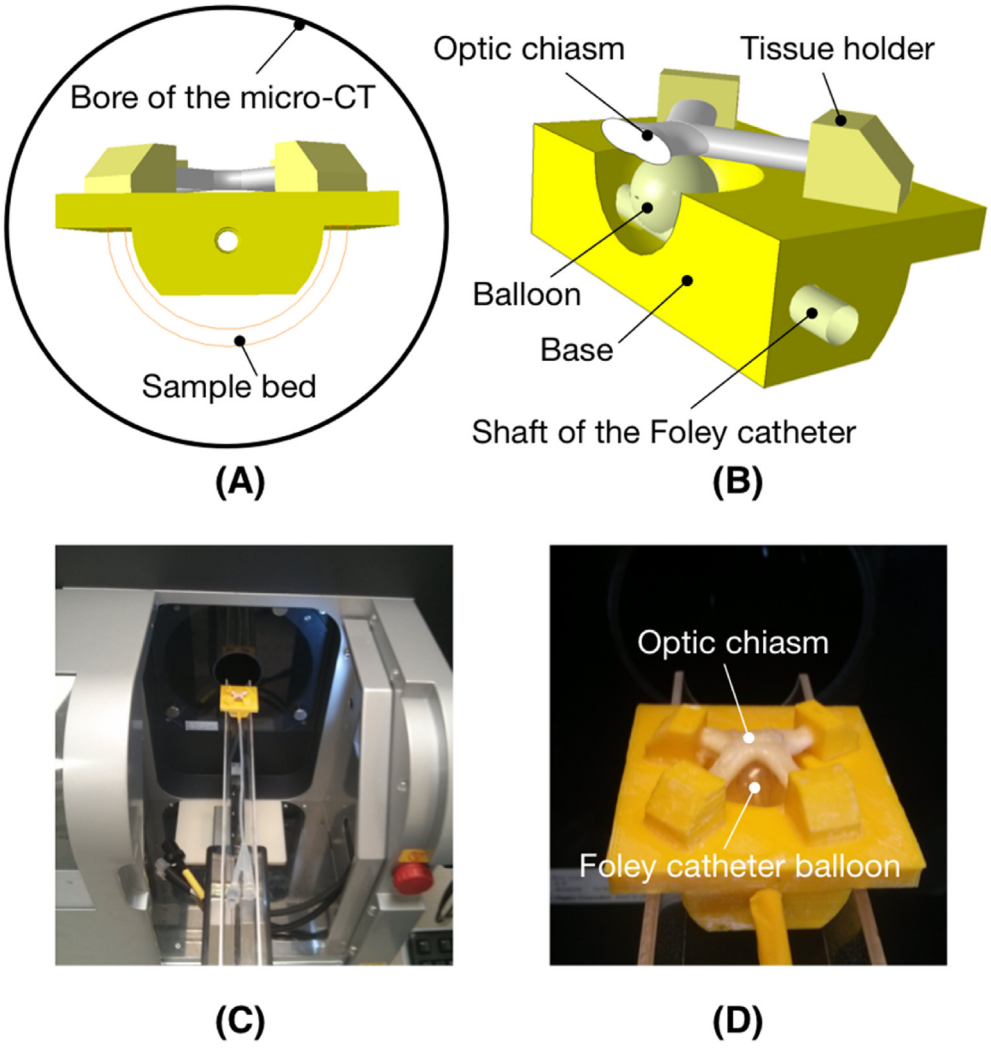

Fig. 1. Experimental setup for *ex vivo* chiasmal compression studies. (**A**) Illustration of the experimental setup in the micro-CT scanner; (**B**) design of the mounting apparatus used to secure the optic chiasm; (**C**) mounting apparatus positioned on the sample bed of the micro-CT scanner; (**D**) The chiasm elevated by the expanded balloon of a Foley catheter.

were obtained. This 3D volume scan was designated the 'baseline' scan.

Micro-CT imaging of the deformed chiasm. After scanning the undeformed chiasm, water was injected into the balloon to elevate the chiasm by approximately half its height as this degree of elevation has been shown clinically to result in VF loss [9]. After around 30 s, the whole apparatus was re-scanned after the chiasmal elevation. The actual volume of water used to inflate the balloon was measured from the scan data. This 3D volume scan was designated the 'deformed' scan.

2.2. Geometry reconstruction and finite element modelling

3D digital reconstruction of the human chiasm. A digital model was constructed to reflect the geometry of the chiasm and the Foley catheter in the baseline scan. Images obtained from the micro-CT scan were imported into an open-source software package, 3D Slicer [10]. The chiasm and Foley catheter in each slice were segmented automatically using intensity thresholding. In some slices where the boundaries of structures were faint due to the contact between the balloon and the chiasm, structures were delineated manually. The surface mesh generated using 3D Slicer was cleaned, repaired, and smoothed with a commercial CAD package, CATIA V5 (Dassault Systèmes, France). For simplicity, only the balloon and a short segment of the Foley catheter were included in the model. Part of the base was reconstructed to simulate the void that accommodates the balloon. The high resolution (59 μm/voxel) of the micro-CT system allowed an accurate reconstruction of the actual structures (Fig. 2).

A pial sheath of 0.086 mm thickness was added to the surface of the optic chiasm in the model. The value of 0.086 mm was derived from measurements in a separate study [8], but it is noted that pia mater thickness can vary between individuals. The thickness of the Foley catheter and of the balloon were set to 0.4 and 0.12 mm, respectively. The thickness of the balloon was estimated from the geometry of the micro-CT scan.

Biomechanical properties of tissues and balloon. The chiasm used had been fixed in formalin so the parameters describing its material properties were modified. Specifically, material stiffness was increased to 7 times the stiffness of normal nerve tissue and pia mater based on a previous study looking at the effects of fixation [11]. The modified material properties of nerve tissue and pial sheath are listed in Table 1. The balloon was made from silicone so a 3-parameter Mooney-Rivlin model was used as a basis for its hyperelastic material behaviour [12].

Boundaries, loading conditions and meshing. The distal faces of the optic nerve and tracts (black arrows in Fig. 2) were fixed to represent the connection of the tissue to the holders by superglue. The balloon was connected to the catheter, which was fixed at its end (white arrow in Fig. 2). The base was fixed as well. The contact between the balloon and chiasm was considered to be frictionless. The core tissues of the optic nerve, chiasm and tract were bonded to their pial sheath. Pressure was applied via the interior surface of the balloon to inflate it. The chiasm was meshed in ANSYS (v13, Ansys Inc. Canonsburg, PA, USA) with a mixture of 20-node hexahedral elements, 10-node tetrahedral element, and 15-node wedge elements to accommodate the complex geometry and provide a better numerical solution. The pial sheath and other parts of the model were meshed using 3-node or 4-node shell elements. The mesh size was verified through a convergence test.

Comparing FEM with experimental data. To ensure that our FEM model was physiologically realistic, we compared the model with experimental data from part 1 above. As the chiasm was only scanned in undeformed and deformed states in part 1, it was only possible to compare experiment and simulation at one degree of deformation. Deformation was examined in two ways: first, the relationship of the elevation of the chiasm to the change in the balloon size and, second, the envelope of the cross-sectional areas of undeformed and deformed chiasm were compared.

2.3. Micro-scale models with nerve fibre orientations

Using FEM, micro-scale models were developed to include optic nerve fibre crossings to examine the effects of optic chiasm compression at an axonal level.

Geometry of representative volume element models. Micro-scale models were generated using representative volume elements (RVE) (Fig. 3). The RVE was designed to capture the major features of the underlying microstructure of the macroscopic model. ANSYS APDL (Ansys Inc. Canonsburg, PA, USA) was used to generate parametric RVEs that simulated nerve fibres crossing each other at different angles. An individual nerve fibre was considered to be circular in cross-section and to consist of an axon surrounded by a myelin sheath. Nerve fibres were surrounded by extracellular space filled with soft solid materials. Dimensions were varied depending on the crossing angle being simulated. All RVE models were meshed with 10-node tetrahedral elements.

Crossing angles. Although hemidecussation of optic nerve fibres in the optic chiasm is well-recognized, there is still a paucity of data regarding exactly where and how nerve fibres cross each other in the

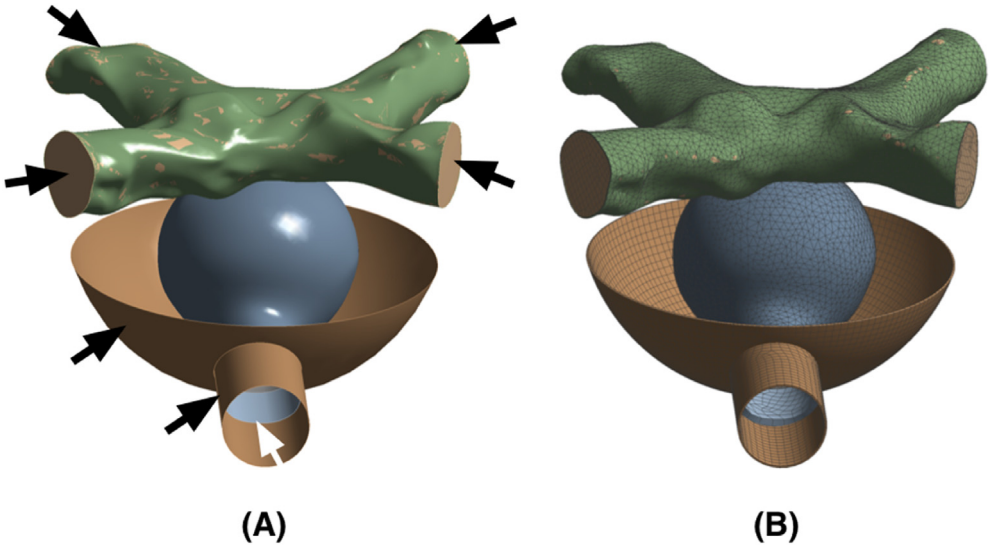

Fig. 2. (**A**) Reconstructed geometry and the boundary constraints of the finite element model. *Black arrows* indicate fixed faces of the optic nerves and tracts; *white arrow* indicates fixed end of the Foley catheter. (**B**) Finite element mesh of the model.

Table 1
Material properties used for chiasmal tissues and balloon.

Tissue	Material model	Material constants	Reference
Pial sheath	Hyperelastic, 2nd Polynomial	C10 = 1.07×10^6 Pa; C01 = -5.03×10^5 Pa; C20 = 8.79×10^7 Pa; C11 = -1.25×10^8 Pa; C02 = 5.09×10^7 Pa	Ho and Kleiven [24]; Metz et al. [11]
Optic nerve	Hyperelastic, Ogden	$\mu_1 = 7308$ Pa; $\alpha_1 = 4.309$; $\mu_2 = 8281$ Pa; $\alpha_2 = 7.736$	Franceschini [16]; Metz et al. [11]
Balloon	Hyperelastic, Mooney-Rivlin	C10 = 0.030 MPa; C01 = −0.182 MPa; C11 = 0.003 MPa	Nagarajan [12]

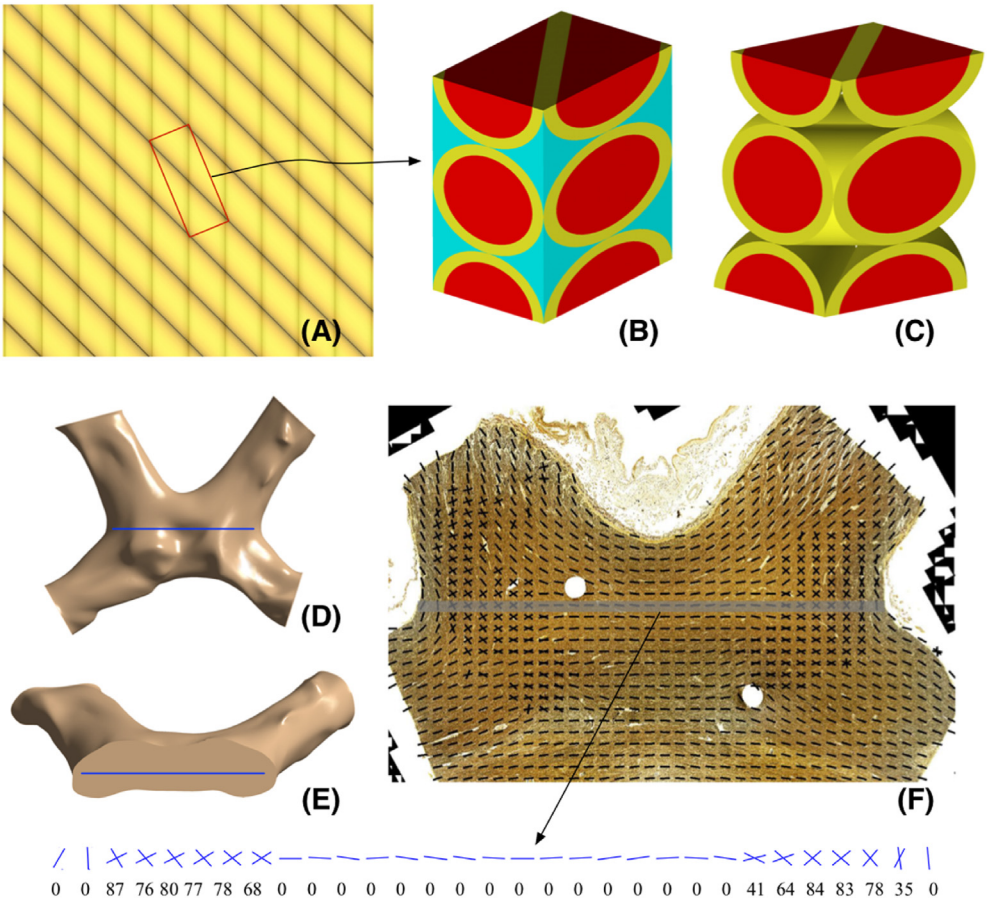

Fig. 3. (**A**) Illustration of fibres crossing; (**B**) representative volume element (RVE) for fibres crossing at a particular angle; (**C**) RVE model without extracellular compartment to show the internal structure. (**D, E**) A coronal section was defined in the macroscopic chiasmal model and the strain values were extracted along this path; (**F**) fibre orientations and crossings obtained from a coronal section of another optic chiasm with crossing angles listed below the orientation plot in degrees. Construction of the RVE models was based on the location and crossing angles in (**F**) and strains extracted from the macroscopic model (**D, E**) were applied to these RVE models.

chiasm. The crossing locations and angles used in this study were derived from a previous study using photomicrographic image processing [8]. A middle slice of the chiasm was selected from this paper as being representative (Fig. 3F).

Material properties of the RVE model. There is little information relating to the material properties of the various components of the RVEs. Myelin sheaths are formed by oligodendrocytes, one of several types of glial cell in the central nervous system. Previous studies have shown that glial cells are softer than axons by a factor of 2–3 [13–15]. For simplicity, the material properties of axons were considered to be the same as those obtained from macro-scale nerve tissues [16] and a three-times softer material stiffness was used to represent the myelin sheath. We assumed that the extracellular space was mostly filled by fluid-like material, simulated as a soft material which was nearly incompressible and which had a very low shear modulus [17]. The material parameters used in the RVE model are listed in Table 2.

Boundary conditions applied to RVEs. RVEs can be stacked together to form a macro structure. Therefore, periodic boundary conditions were applied to ensure that there was no overlap or separation between neighboring RVEs after deformation. Detailed procedures can be found elsewhere [5]. Here, strain tensors of ROIs along a path around the centre of the chiasm were extracted from the macroscopic chiasmal model and applied to the RVEs as boundary conditions (Fig. 3).

Table 2
Ogden hyperelastic constants used in the RVE models.

Tissue	μ_1 (Pa)	μ_2 (Pa)	α_1	α_2
Axon[a]	1044.0	1183.0	4.309	7.736
Myelin sheath[b]	348.0	394.3	4.309	7.736
MECS[c]	52.2	59.2	4.309	7.736

[a] From reference [16].
[b] modified to be 1/3 the stiffness of the axon material model.
[c] modified to be 1/20 the stiffness of the axon material model.

2.4. Output measurement

There is ongoing discussion regarding which mechanical parameter is most representative when considering nerve damage [18]. In the macroscopic chiasmal model presented here, average von Mises strains

were reported along a left–right axis in a coronal cross-section of the chiasm to illustrate strain distributions across the chiasm.

In the micro-scale RVE models, the maximum cross-sectional von Mises strain was reported for each ROI. The cross-sectional strain was defined as the average strain across a cross-section of an axon or a myelin sheath. As the myelin sheath is intimately involved in the failure of conduction of nerve fibres [19,20], the corresponding strain values in both axons and myelin sheaths were reported separately.

3. Results

3.1. Quantitative comparison – FEM versus experiment

We measured the catheter volume increase and chiasmal elevation in both experiment and simulation (Table 3). The displacement of the chiasm was measured at a point located at the centre of its lower surface. Table 3 shows that, at approximately the same elevation, the simulated balloon volume was close to that calculated from the experimental data (13% difference).

3.2. Qualitative comparison – FEM versus experiment

The boundaries of the cross-sectional areas in experiment and simulation were compared for both undeformed and deformed conditions in both coronal and sagittal planes. For purposes of comparison, the boundary coordinates of the simulation cross-sectional images were superimposed on the experimental CT scans as “wire frames” (Fig. 4).

Fig. 4A and B shows that, in the coronal cross-section, the simulation boundary was very close to that of the experiment in both undeformed and deformed states. The discrepancy in areas derived from the two techniques for undeformed and deformed states were 5.7% and 7.0%, respectively.

Fig. 4C and D shows a mid-sagittal cross-section. In this plane, the simulation and experimental cross-sectional areas were slightly less in agreement: the non-overlapping area ratios for the undeformed and deformed cases were 6.5% and 16.0%, respectively.

3.3. Chiasmal strain predictions

Fig. 5 shows the von Mises strain distribution across a coronal section through the middle of the chiasm. Each value represents the average of a vertical column extending the entire height of the chiasm at that point, as illustrated in Fig. 5A. The average von Mises strain of each column was then plotted as a function of the column's location along a left-right axis (Fig. 5C). It can be seen that the strains at the paracentral parts of the chiasm were generally higher than those at the periphery.

3.4. Nerve fibre strain predictions

The maximum cross-sectional von Mises strain in both axon and sheath were plotted as a function of their location from left to right and compared with the overall von Mises strains in the macroscopic chiasmal model (Fig. 6A). Strain amplification factor – the ratio of micro-scale level axonal sheath strain to macro-scale level chiasm strain in Fig. 6A – was plotted in Fig. 6**B–C**.

Table 3
Comparison of the results predicted by the simulation and the experimental measurements.

Scenarios	Balloon volume increase	Elevation of the chiasm
Experiment	0.872 mm^3	1.75 mm
Simulation	1.008 mm^3	1.76 mm
Differences	13.49%	0.57%

4. Discussion

Our study combined an *ex vivo* experiment with a FEM simulation to help clarify the biomechanics involved in chiasmal compression from below, and how this might influence the deformation of the chiasm at both macro- and micro-scales. We found that compression of the chiasm induced high strains, particularly in the paracentral parts of the chiasm. Additionally, at an axonal level, the magnitude of strains affecting crossed fibres was greater than those affecting uncrossed fibres.

Our FEM model matched the observed changes on micro-CT scan well in terms of both qualitative and quantitative comparisons, suggesting that it was reasonable, and thus capable of providing insight into the mechanism of nerve damage resulting from chiasmal compression.

The macro-scale model showed that the paracentral parts of the chiasm experienced the highest strains. Interestingly, a recent study by our group [8] has suggested that the paracentral regions are mostly occupied by crossing nasal nerve fibres which represent the temporal VF. High strains in the paracentral regions would therefore explain why the temporal VF is preferentially affected in chiasmal compression [21].

In the micro-scale RVE models, we demonstrated that the nerve fibre sheath experienced larger strain than the corresponding encased axon. This finding may have implications for the exact mechanism whereby strain on nerve fibres results in loss of function. After taking account of micro-scale nerve fibre packing patterns, the maximum cross-sectional sheath strains calculated along a coronal line through the optic chiasm (Fig. 6A), were similar to those of the macro-scale chiasmal model. Based on histology [8] and our current findings, one may infer that, under the same loading condition, the maximum cross-sectional strains affecting crossed fibres are higher than those affecting uncrossed fibres as illustrated by the amplification factor in Fig. 6B and C. Note that, in absolute terms, some uncrossed fibers had larger strains than some crossed fibers. If field loss were simply due to absolute values of strain, nasal visual field (i.e. uncrossed fibres) should be affected, meaning that there would not be the absolute vertical cutoff, or “step”, of VF loss between nasal and temporal fields that is observed clinically.

There are three possible ways to explain the step. First, the macro-scale chiasmal geometry and the micro-scale fibre distributions were obtained from two different samples, which may not have captured the strain disparity in crossed and uncrossed models due to unmatched morphological information at two length scales. Second, factors other than strain may contribute to loss of VF, including axoplasmic stasis, conduction block, demyelination and/or axonal destruction [22]. Third, the simple measure of strain we have used may not be sufficient to determine the final fate of nerve fibres experiencing chiasmal compression. Strain is an engineering term which describes the overall deformation at a point in the tissue but the relation between strain and resulting nerve fibre dysfunction is, unfortunately, not well understood. Moreover, the strain predicted by the current model represents the result of rapid compression and does not take account of nerve fibre remodelling or other effects which might occur under conditions of chronic compression.

It is clear that complete failure of conduction at any single point will disrupt the function of a nerve fibre as a whole. However, it is possible that partial damage at multiple sites might summate and result in failure of nerve conduction, even if the damage at any given individual site would not do this on its own [23]. In our RVE simulations, only the RVEs at single points along one coronal section across the chiasm were investigated. Therefore, these results only reflected the strains at single points along the entire lengths of the various nerve fibres involved. There is no information relating to strains on the same nerve fibres at different locations. We anticipate that, once more detailed anatomical information regarding nerve fibre anatomy in the chiasm becomes available, it will be possible to investigate the effects of chiasmal compression at multiple sites along nerve fibres rather than at single points as in this study.

Traditionally, the crossed fibres were thought to be located in the centre of the chiasm while uncrossed fibres were located laterally.

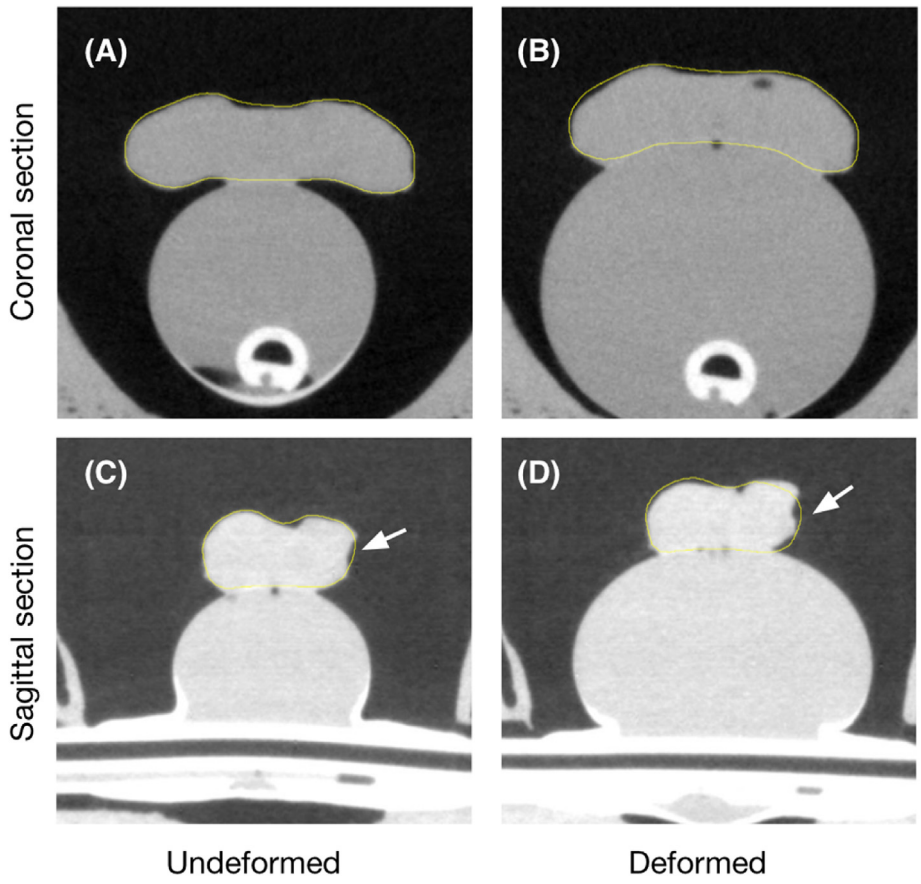

Fig. 4. experimental deformation comparing an image from the micro-CT scan with the predicted deformation from FEM (*yellow wire frame*). Coronal section (**A and B**) and sagittal section (**C and D**) are shown separately. FEM predictions corresponded well to the findings from the micro-CT images.

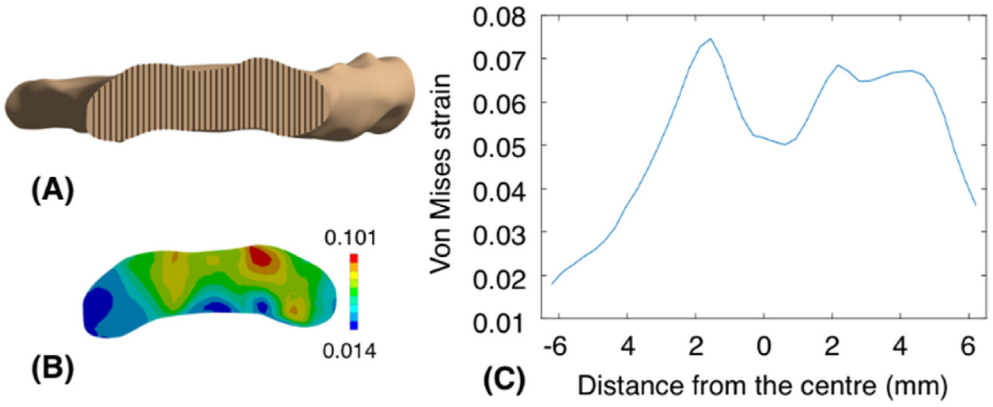

Fig. 5. von Mises strain distribution along a coronal section of the deformed optic chiasm. (**A**) columns used to calculate the strain values in (**C**); (**B**) contour plot of the von Mises strain distribution; (**C**) average cross-sectional von Mises strain from left to right.

However, many fibres in the lateral parts of the chiasm were shown in a previous study to cross (Fig. 3) [8]. If these crossing fibres were derived from the nasal retina even though they were located laterally, they would still experience larger strains than temporal retinal fibres, resulting in preferential loss of temporal visual fields. The precise arrangement of nerve fibres might vary on an individual basis. This, in turn, could affect the precise pattern of VF loss resulting from a given pattern of chiasmal compression and potentially explain some of the inter-subject variability in VF loss noted clinically [9].

In theory, an *in vivo* experiment could provide more precise information relating to what happens during compression of the optic chiasm in humans. However, this is not ethically possible. Granted this, *ex vivo* experiments are useful and, in particular, allow for more precise control of the parameters involved, resulting in much more detailed information. For example, *ex vivo* experiments can provide detailed measurements of pressure, force, strain, and other physical parameters at multiple points, something that would not be possible in an *in vivo* experiment. This particular *ex vivo* experiment, being a pilot study, was not able to provide quantitative validation of all these parameters, particularly because the micro-CT scanner could not provide information related to contrast within the chiasm itself; hence, local internal strain distributions could not be investigated. In future, modification of the micro-CT technique in

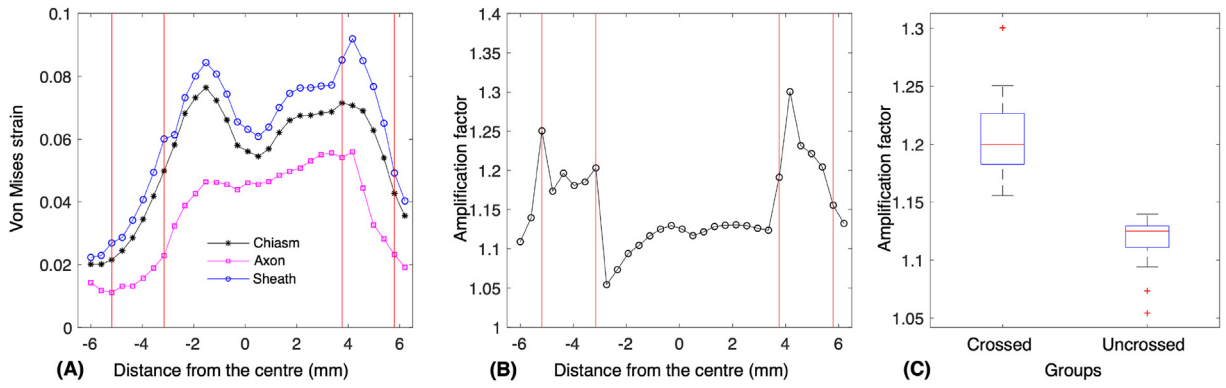

Fig. 6. (**A**) von Mises strains along the path shown in Fig. 3 for different tissues. For axon and sheath, the strain value at each data point was the maximum cross-sectional von Mises strain in each RVE model. The von Mises strains in the macroscopic model along the path, representing the corresponding strain magnitude applied on each RVE model, were also plotted for comparison; (**B**) The strain amplification factor along the path; (**C**) Boxplot of amplification factors in crossed and uncrossed RVEs. Data points between two vertical lines in (**A**) and (**B**) on each side indicate crossed fibres.

order to generate some form of internal contrast, e.g. a speckled pattern in the optic chiasm, would allow calculation of local strains using digital image correlation.

Having said that, the micro-CT results did validate the results of the FEM simulation experiments at a macro level in that there was very good spatial agreement between the chiasmal envelope determined by the two techniques. Given all the assumptions about the geometry, material properties and contact patterns in this complex system, it is very impressive that the model was able to agree with the 'reality' of the *ex vivo* experiment with an error of only 7%. At the very least, this confirms the feasibility of using FEM to model chiasmal compression.

Limitations. Several limitations warrant further discussion. First, the optic chiasm we obtained was preserved in formalin. It is acknowledged that both post-mortem time and fixation significantly affect the mechanical properties of biological tissue [11]. In our simulation, we tried to adjust the material parameters to take account of the expected changes in stiffness resulting from fixation. However, the main aim of this study was to investigate variation of *relative* strain as a function of anatomical location in the chiasm. We believe the relative strain distributions found in this study are likely to represent the *in vivo* situation. A future experiment using fresh tissue, if possible, would provide more representative information regarding the *in vivo* situation in absolute terms.

Second, inflation of a balloon was used in this study to simulate growth of a pituitary tumour. The material properties of a balloon are likely to be very different from those of a real pituitary tumour, and this difference could impact on the findings of the micro-CT study. Moreover, the balloon was expanded over a few minutes, a timing very different to the *in vivo* expansion of a pituitary tumour which typically grows over months to years. There may be many additional factors, e.g. shift of internal water distribution, which influence the ultimate strain distributions in the optic chiasm under conditions of slow compression. Future experimental and FEM studies should aim to investigate and take account of these factors.

Third, information regarding nerve fibre distribution and the results of macroscopic chiasmal loading were actually derived from two separate optic chiasms. It is possible that there could be considerable inter-individual variation in the geometry, material properties, and nerve fibre arrangements of the optic chiasm. This variation could, in turn, result in significant inaccuracies in the strain distributions of a FEM model. However, allowing for this, our model still demonstrated significant differences in the strain distributions between crossed and uncrossed regions, independent of the precise pattern of nerve fibre distribution. It is this difference which is crucial to explaining the origin of the sharp midline vertical 'step' in visual field loss which occurs clinically as a restul of chiasmal compression.

A final point is that, in our RVE model, a single nerve fibre was assumed to be cylindrical with the fibres uniformly distributed and tightly packed. In reality, however, fibre packing patterns are likely to be more complicated. Future studies should take account of more accurate 3D fibre packing patterns once such data become available.

5. Conclusions

Our study combined an *ex vivo* experiment and a FEM model to estimate the strain distribution in the optic chiasm resulting from compression from below. Our model predicted high strains in the paracentral parts of the chiasm, where the nasal fibres have been shown to be located. This effect is consistent with the clinical features of the bitemporal hemian opia. The observed difference in strain between crossed and uncrossed nerve fibres provides an explanation for the clear vertical midline step that seen clinically in these VFs.

Funding sources

Supported by National Natural Science Foundation of China (12002025).

Ethical approval and informed consent (if applicable)

This study was approved by the ACT Health Human Research Ethics Committee (ETH 1.14.020).

Author contribution to study

Xiaofei Wang: Conceptualization, Methodology, Visualization, Writing - Original draft preparation. Andrew J. Neely: Conceptualization, Methodology, Supervision, Writing - Reviewing and Editing. Neeranjali S. Jain: Methodology, Data collection. Swaranjali V. Jain: Methodology, Data collection. Sanjiv Jain: Methodology, Data collection. Murat Tahtali: Methodology, Supervision. Gawn G. McIlwaine: Conceptualization, Methodology. Christian J. Lueck: Conceptualization, Methodology, Supervision, Writing - Reviewing and Editing. All authors have approved the final manuscript.

Declaration of competing interest

The authors declare that there are no conflicts of interest.

Acknowledgments

The authors gratefully acknowledge Dr. Thomas P. Lillicrap and Ms Cathy Gillespie for the valuable discussions and assistance.

References

[1] Kosmorsky GS, Dupps Jr WJ, Drake RL. Nonuniform pressure generation in the optic chiasm may explain bitemporal hemianopsia. Ophthalmology 2008;115:560–5. https://doi.org/10.1016/j.ophtha.2007.07.004.

[2] Hedges TR. Preservation of the upper nasal field in the chiasmal syndrome: an anatomic explanation. Trans Am Ophthalmol Soc 1969;67:131–41.

[3] Bergland R, Ray BS. The arterial supply of the human optic chiasm. J Neurosurg 1969;31:327–34.

[4] McIlwaine GG, Carrim ZI, Lueck CJ, Chrisp TM. A mechanical theory to account for bitemporal hemianopia from chiasmal compression. J Neuro Ophthalmol 2005;25:40–3.

[5] Wang X, Neely AJ, McIlwaine GG, Lueck CJ. Multi-scale analysis of optic chiasmal compression by finite element modelling. J Biomech 2014;47:2292–9. https://doi.org/10.1016/j.jbiomech.2014.04.040.

[6] Wang X, Neely AJ, McIlwaine GG, Tahtali M, Lillicrap TP, Lueck CJ. Finite element modeling of optic chiasmal compression. J Neuro Ophthalmol 2014;34:324–30. https://doi.org/10.1097/WNO.0000000000000145.

[7] Wang X, Neely AJ, McIlwaine GG, Lueck CJ. Biomechanics of chiasmal compression: sensitivity of the mechanical behaviors of nerve fibers to variations in material property and geometry. Int J Comput Methods Eng Sci Mech 2016;17:165–71. https://doi.org/10.1080/15502287.2015.1084069.

[8] Jain NS, Jain SV, Wang X, Neely AJ, Tahtali M, Jain S, et al. Visualization of nerve fiber orientations in the human optic chiasm using photomicrographic image analysis. Invest Ophthalmol Vis Sci 2015;56:6734–9. https://doi.org/10.1167/iovs.15-17443.

[9] Boland MV, Lee IH, Zan E, Yousem DM, Miller NR. Quantitative analysis of the displacement of the anterior visual pathway by pituitary lesions and the associated visual field loss. Invest Ophthalmol Vis Sci 2016;57:3576–80. https://doi.org/10.1167/iovs.16-19410.

[10] Pieper S, Lorensen B, Schroeder W, Kikinis R. The NA-MIC Kit: ITK, VTK, pipelines, grids and 3D slicer as an open platform for the medical image computing community. IEEE; 2006. p. 698–701.

[11] Metz H, McElhaney J, Ommaya AK. A comparison of the elasticity of live, dead, and fixed brain tissue. J Biomech 1970;3:453–8.

[12] Nagarajan P. Rapid production of polymer microstructures. Georgia Institute of Technology; 2008.

[13] Arbogast KB, Margulies SS. A fiber-reinforced composite model of the viscoelastic behavior of the brainstem in shear. J Biomech 1999;32:865–70.

[14] Lu YB, Franze K, Seifert G, Steinhauser C, Kirchhoff F, Wolburg H, et al. Viscoelastic properties of individual glial cells and neurons in the CNS. P Natl Acad Sci USA 2006;103:17759–64. https://doi.org/10.1073/pnas.0606150103.

[15] Shreiber D, Hao H, Elias R. Probing the influence of myelin and glia on the tensile properties of the spinal cord. Biomech Model Mechanobiol 2009;8:311–21. https://doi.org/10.1007/s10237-008-0137-y.

[16] Franceschini G. The mechanics of human brain tissue. Trentino, Italy: University of Trento; 2006.

[17] Chafi MS, Dirisala V, Karami G, Ziejewski M. A finite element method parametric study of the dynamic response of the human brain with different cerebrospinal fluid constitutive properties. Proc Inst Mech Eng H 2009;223:1003–19. https://doi.org/10.1243/09544119jeim631.

[18] Sigal IA, Flanagan JG, Tertinegg I, Ethier CR. Predicted extension, compression and shearing of optic nerve head tissues. Exp Eye Res 2007;85:312–22. https://doi.org/10.1016/J.Exer.2007.05.005.

[19] LaPlaca MC, Simon CM, Prado GR, Cullen DK. CNS injury biomechanics and experimental models. Prog Brain Res 2007;161:13–26. https://doi.org/10.1016/S0079-6123(06)61002-9.

[20] Shi R, Pryor JD. Pathological changes of isolated spinal cord axons in response to mechanical stretch. Neuroscience 2002;110:765–77. https://doi.org/10.1016/S0306-4522(01)00596-6.

[21] Anderson JR, Antoun N, Burnet N, Chatterjee K, Edwards O, Pickard JD, et al. Neurology of the pituitary gland. J Neurol Neurosurg Psychiatr 1999;66:703–21.

[22] Danesh-Meyer HV, Yoon JJ, Lawlor M, Savino PJ. Visual loss and recovery in chiasmal compression. Prog Retin Eye Res 2019;73:100765. https://doi.org/10.1016/j.preteyeres.2019.06.001.

[23] Upton AR, McComas AJ. The double crush in nerve entrapment syndromes. Lancet 1973;2:359–62. https://doi.org/10.1016/s0140-6736(73)93196-6.

[24] Ho J, Kleiven S. Can sulci protect the brain from traumatic injury? J Biomech 2009;42:2074–80. https://doi.org/10.1016/j.jbiomech.2009.06.051.